Research Article

Nano Research
2022, 15(9): 8442–8450

ISSN 1998-0124 CN 11-5974/O4
https://doi.org/10.1007/s12274-022-4463-7

Efficiently band-tailored type-III van der Waals heterostructure for tunnel diodes and optoelectronic devices

Xiangna Cong[1,2], Yue Zheng[1], Fu Huang[1], Qi You[1], Jian Tang[1], Feier Fang[1], Ke Jiang[1], Cheng Han[1] (✉), and Yumeng Shi[1]

[1] *International Collaborative Laboratory of 2D Materials for Optoelectronics Science and Technology of Ministry of Education, Institute of Microscale Optoelectronics, Shenzhen University, Shenzhen 518060, China*

[2] *Key Laboratory of Optoelectronic Devices and Systems of Ministry of Education and Guangdong Province, College of Physics & Optoelectronic Engineering, Shenzhen University, Shenzhen 518060, China*

Received: 16 February 2022 / **Revised:** 6 April 2022 / **Accepted:** 22 April 2022

ABSTRACT

Broken-gap (type-III) two-dimensional (2D) van der Waals heterostructures (vdWHs) offer an ideal platform for interband tunneling devices due to their broken-gap band offset and sharp band edge. Here, we demonstrate an efficient control of energy band alignment in a typical type-III vdWH, which is composed of vertically-stacked molybdenum telluride ($MoTe_2$) and tin diselenide ($SnSe_2$), via both electrostatic and optical modulation. By a single electrostatic gating with hexagonal boron nitride (h-BN) as the dielectric, a variety of electrical transport characteristics including forward rectifying, Zener tunneling, and backward rectifying are realized on the same heterojunction at low gate voltages of ±1 V. In particular, the heterostructure can function as an Esaki tunnel diode with a room-temperature negative differential resistance. This great tunability originates from the atomically-flat and inert surface of h-BN that significantly suppresses the interfacial trap scattering and strain effects. Upon the illumination of an 885 nm laser, the band alignment of heterojunction can be further tuned to facilitate the direct tunneling of photogenerated charge carriers, which leads to a high photocurrent on/off ratio of > 10^5 and a competitive photodetectivity of 1.03 × 10^{12} Jones at zero bias. Moreover, the open-circuit voltage of irradiated heterojunction can be switched from positive to negative at opposite gate voltages, revealing a transition from accumulation mode to depletion mode. Our findings not only promise a simple strategy to tailor the bands of type-III vdWHs but also provide an in-depth understanding of interlayer tunneling for future low-power electronic and optoelectronic applications.

KEYWORDS

broken-gap (type-III) heterostructure, band tailoring, single electrostatic gating, infrared photodetector, photovoltaic effects

1 Introduction

Two-dimensional (2D) semiconductors and their van der Waals heterostructures (vdWHs) provide a promising material family for either exploring novel physics phenomena or breaking through the technological bottlenecks in the post Moore era [1, 2]. The week interlayer vdW interaction allows the scaling-down of 2D crystals to atomically-thin layers and the vertical stack of them into heterostructures with atomically-sharp interfaces regardless of lattice mismatch [3, 4]. The absence of dangling bonds on the 2D surface leads to the sharp band edges with minimal trapping states at the hetero-interface, which enables a variety of electronic and optoelectronic applications of 2D vdWHs in tunnel field-effect transistors (TFETs) [5–7], p–n diodes [8–10], memory devices [11–13], photodetectors [14–19], and photovoltaic cells [20–24]. 2D semiconductors possess a wide range of bandgap and electron affinity, thus establishing the heterostructures with three possible types of energy band alignment: straddling-gap (type-I), staggered-gap (type-II), and broken-gap (type-III) [25]. Compared to type-I and -II vdWHs that are widely utilized in light-emitting and photovoltaic devices respectively [26–28], type-III vdWHs are featured by a nonoverlapping band offset between two semiconductors, which facilitate the charge carrier transport from one energy band to another via a quantum tunneling process [29, 30]. This band-to-band tunneling (BTBT) makes type-III vdWHs well suited for tunnel devices like TFETs or Esaki diodes with high-speed operation and low-power consumption.

The carrier transport across the vdWHs (e.g., tunneling or thermionic emission) in principle depends on not only interlayer band offset but also interfacial band bending that is determined by the Fermi level difference between two semiconductors. In order to realize various transport characteristics or device functionalities in a heterostructure with fixed material choice, it is highly desired to modulate the Fermi level or band structure of 2D semiconductors in a controlled manner. A number of methodologies including thickness modulation [31–34], chemical doping [35, 36], and electrostatic gating [37–40], have been employed to tailor the band alignment of type-II or -III vdWHs for achieving a series of tunnel devices. The thickness modulation applies to 2D semiconductors with thickness-sensitive energy levels, e.g., black phosphorus (BP), and the exact control of flake thickness is not tenable by the conventional mechanical

Address correspondence to hancheng@szu.edu.cn

exfoliation. In addition, the substitutional doping of 2D monolayers via a chemical vapor deposition process has been reported to form the heterostructures with different tunneling behaviors [36]. Nevertheless, this doping process involves complex chemical environment that may introduce undesired impurities or defects at the hetero-interface, thereby limiting the device performance.

Electrostatic gating is considered as a reliable and efficient strategy to tune the band alignment of 2D vdWHs. In a pioneering work, Roy et al. reported a dual-gate control of tungsten diselenide/molybdenum disulfide (WSe_2/MoS_2) heterojunction to obtain distinct tunnel diodes and negative differential resistance (NDR) at low temperatures [38]. This dual-gate architecture requires a complicated fabrication process, and the device performance is restricted by the presented type-II band offset. Recently, several type-III vdWHs [29, 30, 41–43] have been built up based on different combinations of 2D semiconductors such as BP, molybdenum telluride ($MoTe_2$), WSe_2, and tin diselenide ($SnSe_2$), which can easily achieve room-temperature NDR by applying a single gate, in contrast to type-II counterparts. However, most of these reports utilized conventional SiO_2 or high-k metal oxides as the gate dielectric, which would induce interfacial trapping states or strains and thus limit the tunneling efficiency in heterostructures. The interface control has also been demonstrated in $WSe_2/SnSe_2$ heterojunction by constructing heterostructures in inert gas environment [42], and unfortunately different diode behaviors and optoelectronic applications were not reported.

In this work, we demonstrate an all-2D-based device architecture on type-III $MoTe_2/SnSe_2$ heterojunctions by using hexagonal boron nitride (h-BN) and graphene as the dielectric and bottom gate, respectively. The atomically-flat and inert surface of h-BN can significantly suppress the trap scattering and strain effects at hetero-interfaces, which leads to the realization of a series of tunnel diodes at low gate voltages (e.g., ±1 V), including forward rectifying diode, Zener diode, backward rectifying diode, and Esaki diode. In addition, the heterostructure can function as a self-powered infrared photodetector with a high photocurrent on/off ratio of > 10^5 and a competitive detectivity of 1.03×10^{12} Jones under the excitation of an 885 nm laser, benefiting from the direct tunneling (DT) of photogenerated charge carriers across the heterojunction. Furthermore, the open-circuit voltage of heterostructure can be tuned from positive to negative at opposite gate voltages, indicating a switching from accumulation mode to depletion mode.

2 Methods

2.1 Sample preparation and device fabrication

A few-layer graphene sheet was first mechanically exfoliated from graphite crystals (HQ Graphene) by using Scotch tape and subsequently transferred onto a degenerately p-doped Si wafer with 300 nm SiO_2. A h-BN nanosheet was then isolated on a viscoelastic stamp (polydimethylsiloxane (PDMS)) attached on a glass slide, which was precisely transferred onto the graphene by using a transfer station equipped with the metallographic microscope (METATEST E1-M). Using the similar method, $MoTe_2$ and $SnSe_2$ flakes were sequentially prepared and transferred on the top of h-BN layer to create the vertically-stacked $SnSe_2/MoTe_2$/h-BN/graphene heterostructure. After locating the heterostructure under a high-resolution optical microscope (Nikon Eclipse LV150N), a polymethyl methacrylate (PMMA) photoresist layer was carefully spin-coated on the substrate at a maximal speed of 2,000 rpm to avoid the spin-induced rolling of 2D nanosheets. The conventional e-beam lithography (EBL) technique (Raith, PIONEER Two) was subsequently employed to pattern the source and drain electrodes exactly on the $MoTe_2$ and $SnSe_2$ flakes. A 10/50 nm Pd/Au layer was deposited onto the substrate as metal contacts using an e-beam evaporation system (ASB-EPI-C6), followed by a lift-off process in acetone and isopropanol.

2.2 Characterizations and device measurements

Atomic force microscopy (AFM) characterizations were carried out in a Bruker Dimension Icon instrument (BRUKERMultiMode 8) to obtain the morphological images of samples. Raman spectra were measured in a Witec Alpha 300 instrument with a 532 nm laser as the excitation source. The electrical and photoelectrical measurements (including temperature-dependent measurement) were performed by using a probe station (METATEST ScanPro Advance) configured with a Keithley-2636B Source Measure Unit parameter analyzer. An 885 nm laser (filtered from a super-continuous white laser, NKT Photonics FIU-15) modulated by an optical chopper was used to illuminate the device. In addition, the light intensity was measured by a light power meter (Hopoo Color, OHSP-350Z). The transient photoresponse was obtained by a DMM7510 71-bit graphic sampling multimeter. The current noise of photodetectors was measured by a phase-locked amplifier (Stanford Research Systems, SR830) at a gate voltage of –1 V.

3 Results and discussion

The band structures of exfoliated $MoTe_2$ and $SnSe_2$ flakes have been reported in Refs. [41, 43], which are schematically drawn in Fig. 1(a) (left panel). The sizeable offset between the valence band of $MoTe_2$ and conduction band of $SnSe_2$ presents a typical type-III band alignment, and the Fermi level position with reference to energy bands indicates the intrinsic p- and n-type conduction for $MoTe_2$ and $SnSe_2$, respectively. After the contact, the electrons in $MoTe_2$ transfer to $SnSe_2$ (or holes in $SnSe_2$ transfer to $MoTe_2$) due to the Fermi level difference (Fig. 1(a) (right panel)), which results in local band bending in the depletion region to the opposite direction. Thus, $MoTe_2/SnSe_2$ heterostructures were constructed to explore the interfacial engineering of band alignment in type-III vdWHs for the realization of high-performance tunnel devices. Few-layer graphene, h-BN, $MoTe_2$, and $SnSe_2$ nanosheets were sequentially stacked onto the SiO_2/Si substrate to form the heterostructure, on which three-terminal field-effect transistors (FETs) were fabricated using h-BN and graphene as the dielectric and bottom gate, respectively, as schematically illustrated in Fig. 1(b) (details see Methods). The corresponding optical microscopy image of the device is presented in Fig. 1(c), and no obvious bubbles were observed within the stacked area of heterostructure, suggesting the good interface quality. The inset of Fig. 1(d) displays the AFM image of selected region in Fig. 1(c), where the line profiles indicate the thicknesses of ~ 12 and ~ 65 nm for $MoTe_2$ and $SnSe_2$, respectively (Fig. 1(d)). The thickness is comparable to the flakes used in Refs. [41, 43], validating the proposed band structures in Fig. 1(a). The thickness of h-BN in Fig. 1(c) was further determined to ~ 8.7 nm by the AFM characterization (Fig. S1 in the Electronic Supplementary Material (ESM)). Raman spectra of $MoTe_2/SnSe_2$ heterojunction exhibit four characteristic peaks located at ~ 113, ~ 187, ~ 234, and ~ 291 cm^{-1}, as shown in Fig. 1(e), which correspond to the vibration modes of E_g, and A_{1g} from $SnSe_2$ and E_{2g}, and B_{2g} from $MoTe_2$, respectively. Compared to the Raman modes of individual flakes, all the peak position almost remains, and the intensity of $MoTe_2$ signals is largely attenuated due to the strong absorption of incident light by the top $SnSe_2$.

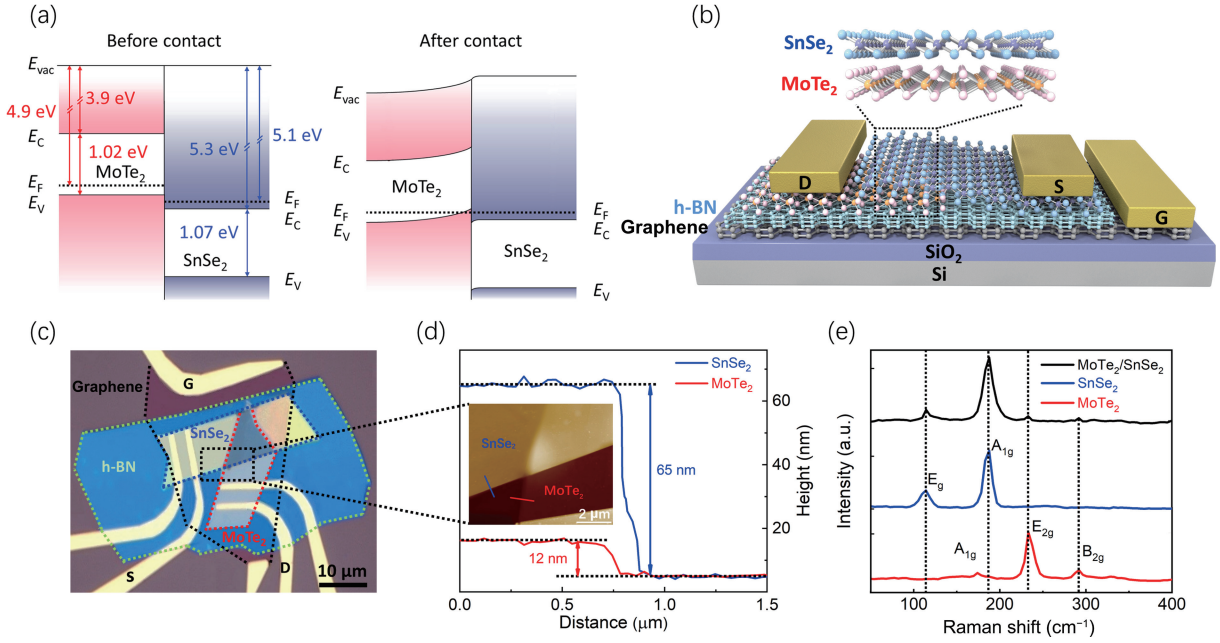

Figure 1 Characterizations of $MoTe_2/SnSe_2$ heterostructure. (a) Schematic band alignments between $MoTe_2$ and $SnSe_2$ before (left panel) and after (right panel) the contact. (b) Schematic illustration of the $MoTe_2/SnSe_2$ FET with h-BN dielectric and graphene back-gate. (c) Optical microscopy image of a typical as-fabricated $MoTe_2/SnSe_2$ device. $MoTe_2$, $SnSe_2$, h-BN, and graphene are marked by the red, blue, green, and black polygons, respectively. (d) AFM height profiles of the $MoTe_2$ and $SnSe_2$ flakes in the inset. Inset: AFM image of the black-dashed rectangular area in (c). (e) Raman spectra of $MoTe_2$, $SnSe_2$, and $MoTe_2/SnSe_2$ heterojunction.

The transport characteristics of individual $MoTe_2$ (p-type) and $SnSe_2$ (n-type) were firstly obtained to confirm their carrier type (Fig. S4 in the ESM). Taking advantage of the type-III band offset, a variety of tunneling transport characteristics were achieved on the $MoTe_2/SnSe_2$ heterostructure with a single gate modulation. The carrier concentration or Fermi level of $MoTe_2$ can be effectively tuned by the electrostatic gating to acquire different diode behaviors, in contrast to conventional p–n diodes based on the semiconductors with certain doping concentration. As shown in Figs. 2(a)–2(c), three types of diodes including forward rectifying diode, Zener diode, and backward rectifying diode were successfully realized on the same heterostructure by applying the gate voltage of 1, 0, and −1 V, respectively. The rectification ratio for these diodes was statistically extracted over devices and plotted in the inset of Fig. 2(b), which shows the ratio of $(8.1 \pm 7.5) \times 10^3$ and $(1.4 \pm 0.7) \times 10^{-3}$ with the highest value of 1.5×10^4 and 6.1×10^{-4} for the forward and backward diodes, respectively (Fig. S5 in the ESM), which is comparable to that of conventional Si, and Ge backward diodes [44–46]. Notably, for Zener diodes, the reverse breakdown can be attributed to Zener tunneling when the breakdown voltage is lower than $4E_g/q$ [32], where E_g and q are the bandgap of semiconductor and the charge of electron, respectively. Realizing Zener and backward rectifying diodes is generally regarded as the initial stage to acquire the tunneling transport of TFETs, and they hold the promising applications in analog circuits and detectors for small signals. On the other hand, the $MoTe_2/SnSe_2$ heterojunction directly stacked on SiO_2/Si substrate presents a dramatically-weakened rectifying behavior compared to the heterojunction on h-BN (Fig. S6 in the ESM), which originates from the significant charge trapping and interlayer strain induced by the rough and dangling-bond-rich surface of oxides. Thus, the realization of all the diodes at low gate voltages reveals the effective modulation of band alignment between $MoTe_2$ and $SnSe_2$ due to the highly-improved interfaces and gating efficiency enabled by h-BN.

The interfacial band alignment of $MoTe_2/SnSe_2$ heterojunction under different gate voltages is schematically illustrated in Figs. 2(e)–2(g) to understand the underlying mechanism. For the forward rectifying diode ($V_g > 0$ V), the Fermi level (E_F) of heterojunction shifts toward the conduction band minimum (CBM, E_c) of $MoTe_2$ due to the electron accumulation at the h-BN/$MoTe_2$ interface (Fig. 2(e)). At a reverse drain–source bias ($V_{ds} < 0$ V), nearly no electrons transfer across the $MoTe_2/SnSe_2$ heterostructure due to the depletion of $MoTe_2$ by the large upward band bending, resulting in an ultralow current. When applying a forward bias ($V_{ds} > 0$ V), the electrons at the CB of $SnSe_2$ can pass through the energy barrier between two CBMs via a tunneling process. The specific tunneling mechanism was further determined by re-plotting the I_{ds}–V_{ds} characteristic of Fig. 2(a) with the Simmons approximation, where DT was obtained at low V_{ds} and Fowler–Nordheim tunneling (FNT) appeared at high V_{ds}. The carrier transport (I–V) of DT and FNT can be described by the following formulas

$$I_{DT} \propto V \exp\left(-\frac{4\pi\sqrt{2m^*\varphi}}{h}\right) \quad (1)$$

$$I_{FNT} \propto V^2 \exp\left(-\frac{8\pi d\sqrt{2m^*\varphi}}{3heV}\right) \quad (2)$$

where d, and φ denote the width and height of tunneling barrier, and m^*, and h are the effective electron mass and Plank constant, respectively. The relationship of $\ln(I_{ds}/V_{ds}^2)$ versus $1/V_{ds}$ was plotted in Fig. 2(d), which presents the linearity with a negative slope for FNT fitting and the exponential rise for DT fitting. The threshold voltage (V_{th}) for FNT was approximately extracted to 0.08 V (1/12.5 V) that corresponds to φ/e, and hence the tunneling barrier was estimated to be ~ 0.08 eV. Different tunneling behaviors can be realized by varying the band alignment at the $MoTe_2/SnSe_2$ interface under different V_{ds} and V_g. For $V_g > 0$ V, small V_{ds} leads to a trapezoidal barrier for DT, while a narrower triangular barrier can be formed at large V_{ds} for FNT. With the decrease of V_g, the E_F downwards shifts to the valence band maximum (VBM, E_v) of $MoTe_2$, which attenuates the upward band bending and thus lifts the E_v of $MoTe_2$ beyond the E_c of $SnSe_2$ at $V_{ds} < 0$ V (Fig. 2(f), left panel). This enables the BTBT of electrons from the VB of $MoTe_2$ to the CB of $SnSe_2$, leading to a

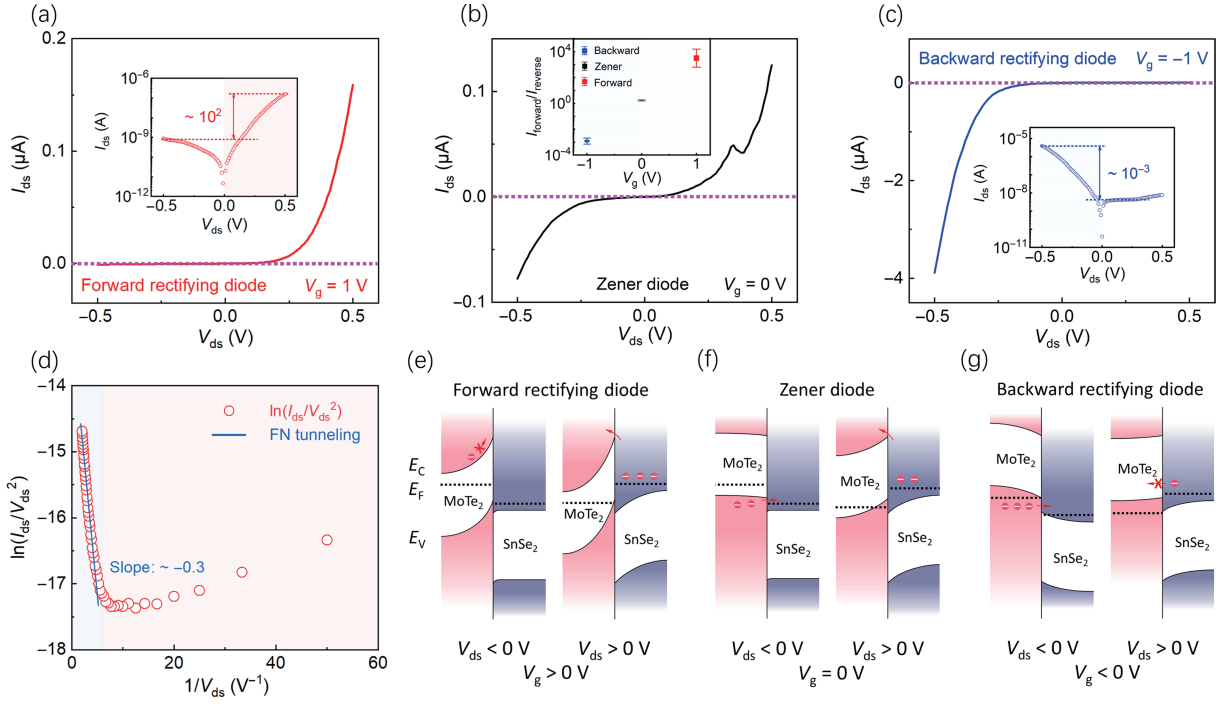

Figure 2 Distinct diode behaviors of $MoTe_2/SnSe_2$ heterostructure. I_{ds}–V_{ds} characteristics of $MoTe_2/SnSe_2$ heterostructure at the gate voltage of (a) 1V, (b) 0 V, and (c) −1 V, respectively. The logarithmic plots at ±1 V are shown in the insets of (a) and (c). The statistically-extracted rectification ratio of different diodes was plotted with respect to V_g in the inset of (b). (d) Fowler–Nordheim plot of $\ln(I_{ds}/V_{ds}^2)$ versus $1/V_{ds}$ from (a). Schematic band alignments of $MoTe_2/SnSe_2$ heterojunction for (e) forward rectifying diode ($V_g > 0$ V), (f) Zener diode ($V_g = 0$ V), and (g) backward rectifying diode ($V_g < 0$ V).

reverse current for the Zener diode. When the V_g is reversed to be negative, the further downward shift of E_F enlarges the reverse current due to the increase of hole concentration in $MoTe_2$, and however the large barrier between two E_c of $MoTe_2$ and $SnSe_2$ drastically limits the forward charge transport at $V_{ds} > 0$ V (Fig. 2(g)), giving rise to a backward rectifying behavior.

NDR, i.e., the decrease of current with increasing bias, is one of the key characteristics of tunnel diodes, and the NDR-based Esaki diodes have shown potential applications in oscillators, high-frequency amplifiers, and multivalued logics [47–51]. The output characteristics of $MoTe_2/SnSe_2$ heterostructure at different negative V_g all exhibit an obvious NDR region nearly located at a low forward bias of 0.3–0.4 V, as shown in Fig. 3(a). The peak current of NDR was enhanced by almost one order to ~ 0.5 μA as increasing V_g to −10 V (a current density of ~ 10 mA·mm^{-2}), which suggests an improved tunneling efficiency due to the increase of available energy states. Generally, the tunneling current is correlated to the density of states (DOS) of each layer and interlayer tunneling probability (T_t) [32], where DOS is considered as a constant for 2D materials [52] and T_t can be estimated by the equation below: $T_t = \exp\left(-2W\sqrt{2m^*(qV_D - E)}/h\right)$, where W and $qV_D - E$ represent the width and height of tunneling barrier, respectively [53]. The use of atomically-flat h-BN with ultralow impurities is supposed to significantly reduce the trapping states and release the strain at the $MoTe_2/SnSe_2$ interface, which can decrease the W with minimized trap scattering and thus produce the high tunneling current as compared to the previous reports using SiO_2 as the dielectric [41, 50, 54].

In order to explore the intrinsic tunneling transport, the $MoTe_2/SnSe_2$ NDR device was measured at low temperatures ranging from 300 to 80 K, and the temperature-dependent I_{ds}–V_{ds} curves at −10 V V_g are shown in Fig. 3(b). The reverse current at $V_{ds} < 0$ V exhibits a weak temperature-dependence because of the insensitivity of BTBT to the thermal activation. Under the forward bias, the NDR region became more obvious with a decreasing current when the temperature was reduced. This can be understood by the suppression of thermionic emission at low temperatures that explicitly contributes to the forward current and weakens the NDR behavior due to the thermally-excited broadening of carrier distribution and the phonon scattering in 2D layers. To further analyze the NDR performance of $MoTe_2/SnSe_2$ device, the peak-to-valley current ratio (PVCR) was extracted and plotted as a function of gate voltage and temperature in Fig. 3(c). The PVCR was found to be remarkably increased from 1.1 at 300 K to 2.3 at 80 K under the same V_g of −10 V. The peak current (I_{peak}) is associated with both tunneling current (I_{tunnel}) and diffusion current ($I_{diffusion}$), where $I_{diffusion}$ is decreased with reducing temperature due to the shorter tail of Fermi–Dirac function. By contrast, the valley current (I_{valley}) is dominated by the $I_{diffusion}$ that is proportional to the temperature, which results in the enhanced PVCR at low temperatures. In addition, the PVCR of $MoTe_2/SnSe_2$ device was nearly unchanged when increasing V_g at room temperature, resulting from the both increase of I_{tunnel} and $I_{diffusion}$. Furthermore, the conductance slope (S) of output curves was inferred by the formula: $S = dV_{ds}/d(\log I_{ds})$. Our device in the reverse bias region shows an average conductance slope of ~ 83 mV·dec^{-1} at room temperature, indicating a fast switching of the rectifier. Based on the S, we further calculated the curvature coefficient (γ), which is an important parameter for high-frequency tunnel diodes and can be expressed as

$$\gamma = \frac{\frac{d^2 I_{ds}}{dV_{ds}^2}}{\frac{dI_{ds}}{dV_{ds}}} | V_{ds} = 0 \quad (3)$$

A curvature coefficient of ~ 74 V^{-1} was achieved at 300 K, which was slightly enhanced to ~ 65 V^{-1} at 80 K, as shown in Fig. 3(d), in agreement with the weak temperature-dependence of BTBT current [25]. This value of γ is comparable to that of Si and III–V semiconductor-based backward diodes [34], thus revealing the potential application of $MoTe_2/SnSe_2$ heterostructures in low-power and high-rectification diodes.

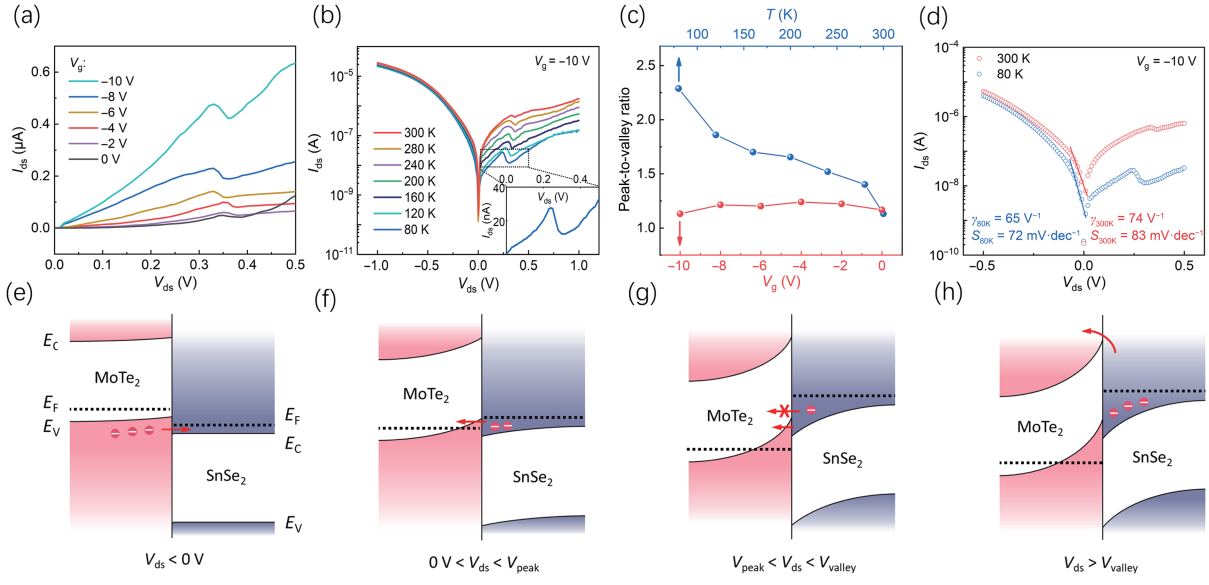

Figure 3 NDR behaviors of $MoTe_2/SnSe_2$ heterostructure. Output characteristics of a $MoTe_2/SnSe_2$ heterostructure with NDR at different (a) gate voltages and (b) temperatures. Inset of (b): the locally-magnified NDR curve at 80 K inside the black box. (c) PVCR of the NDR device as a function of gate voltage and temperature. The statistically-extracted PCVR under different gate voltages was also plotted by error bars in (c). (d) The comparison of output curves at −10 V V_g between 300 and 80 K. The conductance slope (S) and curvature coefficient (γ) can be estimated based on the curve. (e)–(h) Schematic band alignments of $MoTe_2/SnSe_2$ heterojunction with increasing source–drain bias.

The working mechanism of NDR in $MoTe_2/SnSe_2$ heterostructure is demonstrated in the evolution of band structure as a function of source–drain bias, as shown in Figs. 3(e)–3(h). At a reverse bias (V_{ds} < 0 V), electrons directly tunnel from the VB of $MoTe_2$ to the CB of $SnSe_2$, corresponding to the BTBT (Fig. 3(e)). When a small forward bias is applied (0 V < V_{ds} < V_{peak}), the electrons in the CB of $SnSe_2$ immediately tunnel into the VB of $MoTe_2$ owing to the overlap of equivalent energy states (Fig. 3(f)), leading to the increase of current. Following the increase of forward bias, the tunneling current is gradually increased and reaches the maximum with the E_F of $SnSe_2$ aligned with the edge of $MoTe_2$ VB. As the forward bias is increased (V_{peak} < V_{ds} < V_{valley}), the current begins to be reduced because of the decrease of overlap region between the filled states in $SnSe_2$ and empty states in $MoTe_2$, and the E_F of $SnSe_2$ finally lies in the forbidden band of $MoTe_2$ (Fig. 3(g)), which prohibits the tunneling process and thereby leads to the NDR behavior. With the further increase of bias (V_{valley} < V_{ds}), the thermionic emission or thermal-assisted tunneling of majority carriers from the CB of $SnSe_2$ to the CB of $MoTe_2$ dominates the transport across the $MoTe_2/SnSe_2$ heterojunction (Fig. 3(h)), resulting in the re-increase of current.

In addition to the electrostatic gating, the light illumination was also employed to modulate the band alignment of $MoTe_2/SnSe_2$ heterostructure for realizing high-performance optoelectronic devices. The photoresponse of $MoTe_2/SnSe_2$ device was measured under the illumination of an infrared 885 nm laser, as schematically shown in Fig. 4(a), which is consistent with the interfacial barrier of ~ 1.4 eV in the heterojunction (Fig. 1(a)). The obtained I_{ds}–V_{ds} characteristics at V_g = −1 V in the dark and under the light irradiation of various power density are presented in Fig. 4(b), and the negative gate voltage was used to notably lower the dark current at forward bias and thus enhance the photodetection performance. Compared with the dark condition, the irradiated device exhibits a significant current increase by orders of magnitude especially for the positive bias. Furthermore, the I_{ds}–V_{ds} curves at V_{ds} > 0 V can be well fitted by the DT model (Eq. (1)), where the re-plotted $\ln(I_{ds}/V_{ds}^2)$ shows a good linearity with respect to $\ln(1/V_{ds})$ in Fig. 4(c), hence revealing the dominant DT transport. The energy band diagrams of $MoTe_2/SnSe_2$ heterostructure before and after light illumination are illustrated in Fig. 4(d). In the dark, the heterojunction serves as a backward diode in which the electrons cannot tunnel through the interfacial barrier at a forward bias. Upon the light illumination, the excessive charge carriers are generated in both $MoTe_2$ and $SnSe_2$ sides and subsequently accumulated at the interface due to the built-in electric field. This leads to the increase of Fermi level difference between $MoTe_2$ and $SnSe_2$, which facilitates the tunneling of photogenerated electrons from the CB of $SnSe_2$ to the CB of $MoTe_2$ via a DT process. The tunneled electrons are quickly recombined with the accumulated holes in $MoTe_2$, leading to the reduction of the interface trapping.

The $MoTe_2/SnSe_2$ device can function as a self-powered photodetector that works without additional power supplies, which has attracted great attention due to the requirement of low-power consumption for high-performance optoelectronics. To extract the key parameters of this photodetector, the time-dependent photoresponse was measured at zero bias for different light intensity, as shown in Fig. 4(e). The photocurrent (defined as I_{ph} = $I_{illumination}$ − I_{dark}) was significantly increased from 14 to 170 nA with the intensity increased from 2.3 to 92 mW·cm^{-2}. This leads to a remarkably-high current on/off ratio of 10^5–10^6 owing to the ultralow dark current of 10^{-12}–10^{-13} A, which is among the highest reported values in 2D vdWHs [30, 55, 56]. In addition, the photocurrent did not show obvious attenuation after multiple switching of light, suggesting an excellent stability of the photoresponse. The rise (τ_r) and decay time (τ_d) of the photodetector, defined as the time interval of the net photocurrent in the range from 10% to 90%, were estimated to be 10 and 12 ms, respectively (Figs. S8(a) and S8(b) in the ESM), which are comparable to the previous report [57–59]. As an essential parameter of photodetectors, the photoresponsivity (R) was calculated by the Eq. (4) [60]

$$R = \frac{I_{ph}}{P_{in} \times A} \quad (4)$$

where P_{in} and A are the intensity of incident light and the active area of light illumination, respectively. The extracted R was enhanced to 36 A·W^{-1} when decreasing the incident power density to 2.3 mW·cm^{-2} (Fig. 4(f), red line). The specific detectivity (D^*) is the key parameter to characterize the sensitivity of photodetectors,

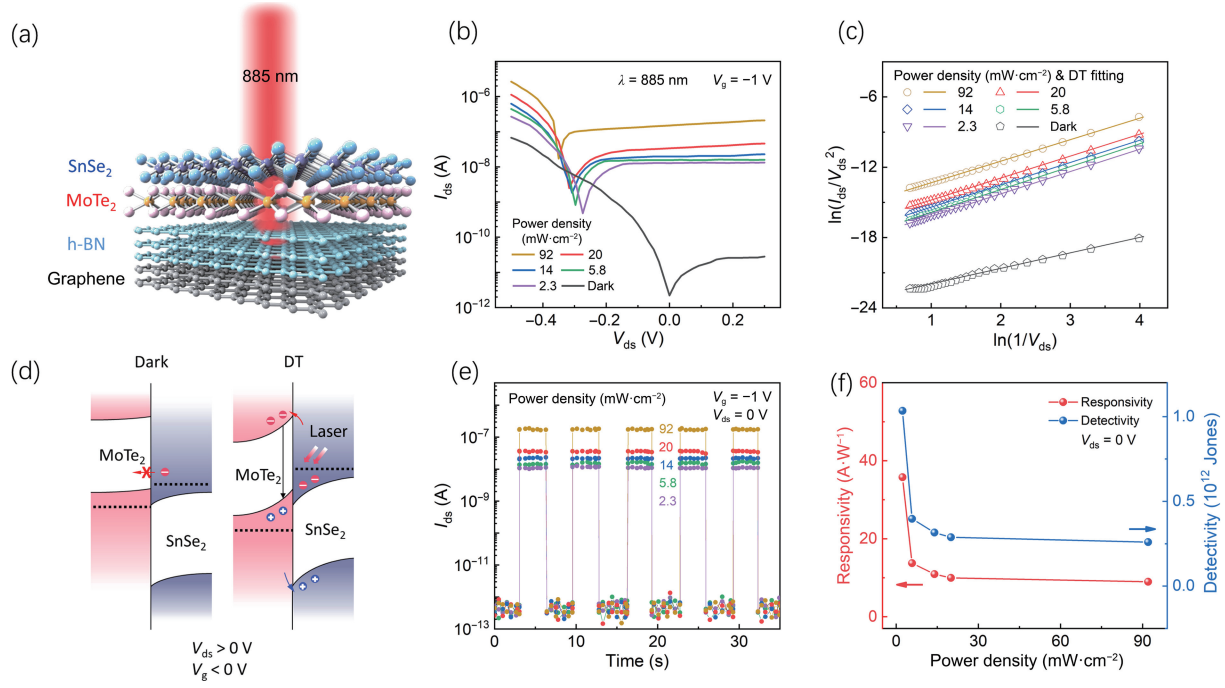

Figure 4 Infrared photodetection of $MoTe_2/SnSe_2$ heterostructure. (a) Schematic of the $MoTe_2/SnSe_2$ photodetector under the illumination of an 885 nm laser. (b) I_{ds}–V_{ds} characteristics with respect to incident laser power density at $V_g = -1$ V. (c) DT plots of $\ln(I_{ds}/V_{ds}^2)$ versus $\ln(1/V_{ds})$ obtained from (b). The solid lines represent DT model fitting of the experimental data. (d) Band alignments of the $MoTe_2/SnSe_2$ heterojunction at $V_g < 0$ V and $V_{ds} > 0$ V without and with the light irradiation. (e) Time-dependent photoresponse of the $MoTe_2/SnSe_2$ device at $V_g = -1$ V and $V_{ds} = 0$ V. (f) Calculated responsivity and detectivity as a function of laser power density at zero bias.

which corresponds to the minimal signal that can be detected from the environment of background noise, as calculated by the following formula [61]

$$D^{\star} = \frac{(AB)^{1/2}}{\mathrm{NEP}} \quad (5)$$

where B is the noise bandwidth and noise equivalent power (NEP) can be expressed as: noise current density/R. The noise power density of our device was measured as a function of frequency (f) (Fig. S8(c) in the ESM), which shows a $1/f$ noise region at low frequency for the extraction of noise current density. As shown in Fig. 4(f) (blue line), the calculated detectivity can reach up to 1.03×10^{12} Jones at the light intensity of 2.3 mW·cm^{-2}. As a result, benefiting from the light-induced modulation of band alignment, the $MoTe_2/SnSe_2$ heterostructure demonstrates a competitive performance for the self-powered infrared photodetection. The comparison of key parameters in tunnel diodes and photodetectors with previous type-II and -III vdWHs is listed in Table S1 in the ESM.

Last but not least, the photovoltaic properties of $MoTe_2/SnSe_2$ heterostructure were investigated to clarify the broken-gap band offset as well as to demonstrate its potential for light-harvesting applications. Figures 5(a) and 5(b) show the output characteristics of $MoTe_2/SnSe_2$ device under the illumination of 885 nm laser as a function of gate voltages. The I_{ds}–V_{ds} curve was found to shift from the second quadrant to the fourth quadrant with the V_g reversed from positive to negative, where the open-circuit voltage (V_{oc}) was varied from −54 mV at 10 V to 17 mV at −10 V (Fig. 5(c)). In general, V_{oc} appears at a positive bias in traditional p–n diodes due to the higher built-in potential in n-type material than that in p-type material. The different behavior in our device originates from the electrostatic modulation of band alignment in the $MoTe_2/SnSe_2$ heterostructure, which results in the transition from an accumulation mode (Fig. 5(a)) to a depletion mode (Fig. 5(b)). The band structure of $MoTe_2/SnSe_2$ heterostructure in the accumulation and depletion mode is illustrated in Figs. 5(e) and 5(f), respectively. When a positive V_g is applied, the Fermi level of $MoTe_2$ upwards shifts, which leads to the accumulation of opposite carriers at the interface and the formation of built-in potential. The photogenerated electrons in $MoTe_2$ or holes in $SnSe_2$ can be dragged out of the junction by the built-in potential, thus resulting in the negative V_{oc}. Similarly, the application of a negative V_g leads to the depletion of interfacial region, which induces a reversed built-in potential and a positive V_{oc}. The obtained V_{oc} and short-circuit current (I_{sc}) were plotted with respect to V_g in Fig. 5(c). To further extract the photovoltaic parameters of our device, I_{ds}–V_{ds} curves were measured at $V_g = 2$ V under various laser power. The output electrical power P_{el} was calculated by the equation $P_{el} = I_{ds}V_{ds}$, which shows the maximum ($P_{el,max}$) nearly at −100 mV V_{oc} (Fig. 5(d)). The power conversion efficiency (η_{pv}) is defined as $\eta_{pv} = P_{el,max}/P_{opt}$, where P_{opt} is the incident optical power. The maximum efficiency was estimated to be ~ 0.4%. The filling factor, defined as $FF = P_{el,max}/(I_{sc}V_{oc})$, was extracted to be ~ 52%, which is clearly improved compared to the previous reports on the negative photovoltaic effect [62–64].

4 Conclusions

In summary, a type-III $MoTe_2/SnSe_2$ heterostructure with h-BN as the dielectric has been efficiently modulated by a single electrostatic gating and light illumination. The $MoTe_2/SnSe_2$ heterojunction can function as the forward rectifying diode, Zener diode, and backward rectifying diode at a low gate voltage of 1 V. A room-temperature NDR behavior was clearly observed at a low bias of ~ 0.35 V, and a peak current density of ~ 10 mA·mm^{-2} was achieved. Under an 885 nm laser irradiation, a $MoTe_2/SnSe_2$ self-powered photodetector was obtained, which presents a high photocurrent on/off ratio over 10^5 and a competitive detectivity of 1.03×10^{12} Jones. In addition, the V_{oc} of irradiated device was switched from positive to negative at opposite gate voltages, revealing the effective control of broken-gap band alignment. Our results promise a simple strategy to efficiently tailor the band

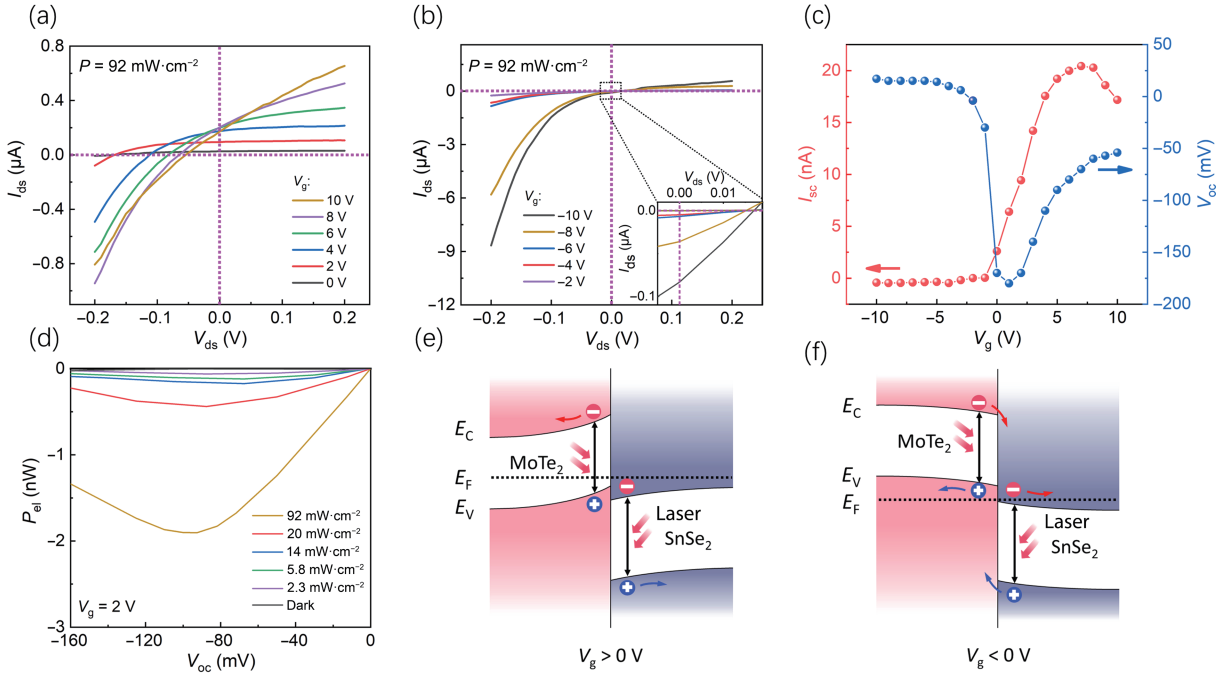

Figure 5 Photovoltaic effects of $MoTe_2/SnSe_2$ heterostructure. I_{ds}–V_{ds} curves under the laser power density of 92 mW·cm^{-2} at different (a) positive and (b) negative gate voltages. Inset: the locally-enlarged curves of the selected area by the black box. (c) The plots of short-circuit current and open circuit voltage as a function of V_g. (d) Output electrical power versus V_{oc} for different power density. Band structure of the $MoTe_2/SnSe_2$ heterojunction under the (e) accumulation mode ($V_g > 0$ V) and (f) depletion mode ($V_g < 0$ V), respectively.

alignment of type-III vdWHs for future low-power electronic and optoelectronic applications.

Acknowledgements

The authors acknowledge the financial support from the National Natural Science Foundation of China (No. 62004128), Fundamental Research Foundation of Shenzhen (No. JCYJ20190808152607389), and the technical support from the Photonics Center of Shenzhen University.

Electronic Supplementary Material: Supplementary material (AFM image for the h-BN layer in Fig. 1(c), diode behaviors of a $MoTe_2/SnSe_2$ heterojunction with a ~ 15 nm-thick h-BN layer, diode behaviors of a ~ 6 nm $MoTe_2$/ ~ 8 nm $SnSe_2$ heterojunction, output and transfer characteristics of a typical $MoTe_2$ and $SnSe_2$ FET, a $MoTe_2/SnSe_2$ diode with the highest rectification ratio, diode behaviors of a $MoTe_2/SnSe_2$ heterojunction fabricated on the SiO_2/Si substrate, transfer characteristic of the device in Fig. 2, dynamic photoresponse of a self-powered $MoTe_2/SnSe_2$ photodetector, comparison of device performance with different type-II and -III vdWHs) is available in the online version of this article at https://doi.org/10.1007/s12274-022-4463-7.

References

[1] Lee, C. H.; Lee, G. H.; van der Zande, A. M.; Chen, W. C.; Li, Y. L.; Han, M. Y.; Cui, X.; Arefe, G.; Nuckolls, C.; Heinz, T. F. et al. Atomically thin p–n junctions with van der Waals heterointerfaces. *Nat. Nanotechnol.* **2014**, *9*, 676–681.

[2] Liang, S. J.; Cheng, B.; Cui, X. Y.; Miao, F. van der Waals heterostructures for high-performance device applications: Challenges and opportunities. *Adv. Mater.* **2020**, *32*, 1903800.

[3] Wang, Q. H.; Kalantar-Zadeh, K.; Kis, A.; Coleman, J. N.; Strano, M. S. Electronics and optoelectronics of two-dimensional transition metal dichalcogenides. *Nat. Nanotechnol.* **2012**, *7*, 699–712.

[4] Cheng, R. Q.; Wang, F.; Yin, L.; Wang, Z. X.; Wen, Y.; Shifa, T. A.; He, J. High-performance, multifunctional devices based on asymmetric van der Waals heterostructures. *Nat. Electron.* **2018**, *1*, 356–361.

[5] Balaji, Y.; Smets, Q.; De La Rosa, C. J. L.; Lu, A. K. A.; Chiappe, D.; Agarwal, T.; Lin, D. H. C.; Huyghebaert, C.; Radu, I.; Mocuta, D. et al. Tunneling transistors based on $MoS_2/MoTe_2$ van der Waals heterostructures. *IEEE J. Electron Devices Soc.* **2018**, *6*, 1048–1055.

[6] Ma, Q.; Andersen, T. I.; Nair, N. L.; Gabor, N. M.; Massicotte, M.; Lui, C. H.; Young, A. F.; Fang, W. J.; Watanabe, K.; Taniguchi, T. et al. Tuning ultrafast electron thermalization pathways in a van der Waals heterostructure. *Nat. Phys.* **2016**, *12*, 455–459.

[7] Balaji, Y.; Smets, Q.; Szabo, Á.; Mascaro, M.; Lin, D.; Asselberghs, I.; Radu, I.; Luisier, M.; Groeseneken, G. $MoS_2/MoTe_2$ heterostructure tunnel FETs using gated Schottky contacts. *Adv. Funct. Mater.* **2020**, *30*, 1905970.

[8] Huang, M. Q.; Li, S. M.; Zhang, Z. F.; Xiong, X.; Li, X. F.; Wu, Y. Q. Multifunctional high-performance van der Waals heterostructures. *Nat. Nanotechnol.* **2017**, *12*, 1148–1154.

[9] Georgiou, T.; Jalil, R.; Belle, B. D.; Britnell, L.; Gorbachev, R. V.; Morozov, S. V.; Kim, Y. J.; Gholinia, A.; Haigh, S. J.; Makarovsky, O. et al. Vertical field-effect transistor based on graphene–WS_2 heterostructures for flexible and transparent electronics. *Nat. Nanotechnol.* **2013**, *8*, 100–103.

[10] Yu, W. J.; Li, Z.; Zhou, H. L.; Chen, Y.; Wang, Y.; Huang, Y.; Duan, X. F. Vertically stacked multi-heterostructures of layered materials for logic transistors and complementary inverters. *Nat. Mater.* **2013**, *12*, 246–252.

[11] Liu, C. S.; Yan, X.; Song, X. F.; Ding, S. J.; Zhang, D. W.; Zhou, P. A semi-floating gate memory based on van der Waals heterostructures for quasi-non-volatile applications. *Nat. Nanotechnol.* **2018**, *13*, 404–410.

[12] Bertolazzi, S.; Krasnozhon, D.; Kis, A. Nonvolatile memory cells based on MoS_2/graphene heterostructures. *ACS Nano* **2013**, *7*, 3246–3252.

[13] Vu, Q. A.; Shin, Y. S.; Kim, Y. R.; Nguyen, V. L.; Kang, W. T.; Kim, H.; Luong, D. H.; Lee, I. M.; Lee, K.; Ko, D. S. et al. Two-terminal floating-gate memory with van der Waals heterostructures for ultrahigh on/off ratio. *Nat. Commun.* **2016**, *7*, 12725.

[14] Kang, B.; Kim, Y.; Yoo, W. J.; Lee, C. Ultrahigh photoresponsive device based on ReS_2/graphene heterostructure. *Small* **2018**, *14*, 1802593.

[15] Yu, W. Z.; Li, S. J.; Zhang, Y. P.; Ma, W. L.; Sun, T.; Yuan, J.; Fu, K.; Bao, Q. L. Near-infrared photodetectors based on

$MoTe_2$/graphene heterostructure with high responsivity and flexibility. *Small* **2017**, *13*, 1700268.
[16] Lu, Z. J.; Xu, Y.; Yu, Y. Q.; Xu, K. W.; Mao, J.; Xu, G. B.; Ma, Y. M.; Wu, D.; Jie, J. S. Ultrahigh speed and broadband few-layer $MoTe_2$/Si 2D-3D heterojunction-based photodiodes fabricated by pulsed laser deposition. *Adv. Funct. Mater.* **2020**, *30*, 1907951.
[17] Wang, F. K.; Luo, P.; Zhang, Y.; Huang, Y.; Zhang, Q. F.; Li, Y.; Zhai, T. Y. Band structure engineered tunneling heterostructures for high-performance visible and near-infrared photodetection. *Sci. China Mater.* **2020**, *63*, 1537–1547.
[18] Lv, L.; Zhuge, F. W.; Xie, F. J.; Xiong, X. J.; Zhang, Q. F.; Zhang, N.; Huang Y.; Zhai, T. Y. Reconfigurable two-dimensional optoelectronic devices enabled by local ferroelectric polarization. *Nat. Commun.* **2019**, *10*, 3331.
[19] Liu, R.; Wang, F. K.; Liu, L. X.; He, X. Y.; Chen, J. Z.; Li, Y.; Zhai, T. Y. Band alignment engineering in two-dimensional transition metal dichalcogenide-based heterostructures for photodetectors. *Small Structures* **2021**, *2*, 2000136.
[20] Pezeshki, A.; Shokouh, S. H. H.; Nazari, T.; Oh, K.; Im, S. Electric and photovoltaic behavior of a few-layer α-$MoTe_2$/MoS_2 dichalcogenide heterojunction. *Adv. Mater.* **2016**, *28*, 3216–3222.
[21] Hu, S. Q.; Xu, J. P.; Zhao, Q. H.; Luo, X. G.; Zhang, X. T.; Wang, T.; Jie, W. Q.; Cheng, Y. C.; Frisenda, R.; Castellanos-Gomez, A. et al. Gate-switchable photovoltaic effect in BP/$MoTe_2$ van der Waals heterojunctions for self-driven logic optoelectronics. *Adv. Opt. Mater.* **2021**, *9*, 2001802.
[22] Chen, Y.; Wang, X. D.; Wu, G. J.; Wang, Z.; Fang, H. H.; Lin, T.; Sun, S.; Shen, H.; Hu, W. D.; Wang, J. L. et al. High-performance photovoltaic detector based on $MoTe_2$/MoS_2 van der Waals heterostructure. *Small* **2018**, *14*, 1703293.
[23] Long, M. S.; Liu, E. R.; Wang, P.; Gao, A. Y.; Xia, H.; Luo, W.; Wang, B. G.; Zeng, J. W.; Fu, Y. J.; Xu, K. et al. Broadband photovoltaic detectors based on an atomically thin heterostructure. *Nano Lett.* **2016**, *16*, 2254–2259.
[24] Bastonero, L.; Cicero, G.; Palummo, M.; Re Fiorentin, M. Boosted solar light absorbance in PdS_2/PtS_2 vertical heterostructures for ultrathin photovoltaic devices. *ACS Appl. Mater. Interfaces* **2021**, *13*, 43615–43621.
[25] Yan, R. S.; Fathipour, S.; Han, Y. M.; Song, B.; Xiao, S. D.; Li, M. D.; Ma, N.; Protasenko, V.; Muller, D. A.; Jena, D. et al. Esaki diodes in van der Waals heterojunctions with broken-gap energy band alignment. *Nano Lett.* **2015**, *15*, 5791–5798.
[26] Chen, W. J.; Liang, R. R.; Zhang, S. Q.; Liu, Y.; Cheng, W. J.; Sun, C. C.; Xu, J. Ultrahigh sensitive near-infrared photodetectors based on $MoTe_2$/germanium heterostructure. *Nano Res.* **2020**, *13*, 127–132.
[27] Furchi, M. M.; Pospischil, A.; Libisch, F.; Burgdörfer, J.; Mueller, T. Photovoltaic effect in an electrically tunable van der Waals heterojunction. *Nano Lett.* **2014**, *14*, 4785–4791.
[28] Koppens, F. H. L.; Mueller, T.; Avouris, P.; Ferrari, A. C.; Vitiello, M. S.; Polini, M. Photodetectors based on graphene, other two-dimensional materials and hybrid systems. *Nat. Nanotechnol.* **2014**, *9*, 780–793.
[29] Na, J.; Kim, Y.; Smet, J. H.; Burghard, M.; Kern, K. Gate-tunable tunneling transistor based on a thin black phosphorus–$SnSe_2$ heterostructure. *ACS Appl. Mater. Interfaces* **2019**, *11*, 20973–20978.
[30] Tan, C. Y.; Yin, S. Q.; Chen, J. W.; Lu, Y.; Wei, W. S.; Du, H. F.; Liu, K. L.; Wang, F. K.; Zhai, T. Y.; Li, L. Broken-gap PtS_2/WSe_2 van der Waals heterojunction with ultrahigh reverse rectification and fast photoresponse. *ACS Nano* **2021**, *15*, 8328–8337.
[31] Lv, Q. S.; Yan, F. G.; Mori, N.; Zhu, W. K.; Hu, C.; Kudrynskyi, Z. R.; Kovalyuk, Z. D.; Patanè, A.; Wang, K. Y. Interlayer band-to-band tunneling and negative differential resistance in van der Waals BP/InSe field-effect transistors. *Adv. Funct. Mater.* **2020**, *30*, 1910713.
[32] Liu, X. C.; Qu, D. S.; Li, H. M.; Moon, I.; Ahmed, F.; Kim, C.; Lee, M.; Choi, Y.; Cho, J. H.; Hone, J. C. et al. Modulation of quantum tunneling via a vertical two-dimensional black phosphorus and molybdenum disulfide p–n junction. *ACS Nano* **2017**, *11*, 9143–9150.
[33] Duong, N. T.; Lee, J.; Bang, S.; Park, C.; Lim, S. C.; Jeong, M. S. Modulating the functions of MoS_2/$MoTe_2$ van der Waals heterostructure via thickness variation. *ACS Nano* **2019**, *13*, 4478–4485.
[34] Nourbakhsh, A.; Zubair, A.; Dresselhaus, M. S.; Palacios, T. Transport properties of a MoS_2/WSe_2 heterojunction transistor and its potential for application. *Nano Lett.* **2016**, *16*, 1359–1366.
[35] Wang, Y. N.; Xiang, D.; Zheng, Y.; Liu, T.; Ye, X.; Gao, J.; Yang, H.; Han, C.; Chen, W. van der Waals heterostructures with tunable tunneling behavior enabled by MoO_3 surface functionalization. *Adv. Opt. Mater.* **2020**, *8*, 1901867.
[36] Fan, S. D.; Yun, S. J.; Yu, W. J.; Lee, Y. H. Tailoring quantum tunneling in a vanadium-doped WSe_2/$SnSe_2$ heterostructure. *Adv. Sci.* **2020**, *7*, 1902751.
[37] Jiang, X. X.; Shi, X. Y.; Zhang, M.; Wang, Y. R.; Gu, Z. H.; Chen, L.; Zhu, H.; Zhang, K.; Sun, Q. Q.; Zhang, D. W. A symmetric tunnel field-effect transistor based on MoS_2/black phosphorus/MoS_2 nanolayered heterostructures. *ACS Appl. Nano Mater.* **2019**, *2*, 5674–5680.
[38] Roy, T.; Tosun, M.; Cao, X.; Fang, H.; Lien, D. H.; Zhao, P. D.; Chen, Y. Z.; Chueh, Y. L.; Guo, J.; Javey, A. Dual-gated MoS_2/WSe_2 van der Waals tunnel diodes and transistors. *ACS Nano* **2015**, *9*, 2071–2079.
[39] Murali, K.; Dandu, M.; Das, S.; Majumdar, K. Gate-tunable WSe_2/$SnSe_2$ backward diode with ultrahigh-reverse rectification ratio. *ACS Appl. Mater. Interfaces* **2018**, *10*, 5657–5664.
[40] Yan, X.; Liu, C. S.; Li, C.; Bao, W. Z.; Ding, S. J.; Zhang, D. W.; Zhou, P. Tunable $SnSe_2$/WSe_2 heterostructure tunneling field effect transistor. *Small* **2017**, *13*, 1701478.
[41] Lee, J.; Duong, N. T.; Bang, S.; Park, C.; Nguyen, D. A.; Jeon, H.; Jang, J.; Oh, H. M.; Jeong, M. S. Modulation of junction modes in $SnSe_2$/$MoTe_2$ broken-gap van der Waals heterostructure for multifunctional devices. *Nano Lett.* **2020**, *20*, 2370–2377.
[42] Fan, S. D.; Vu, Q. A.; Lee, S.; Phan, T. L.; Han, G.; Kim, Y. M.; Yu, W. J.; Lee, Y. H. Tunable negative differential resistance in van der Waals heterostructures at room temperature by tailoring the interface. *ACS Nano* **2019**, *13*, 8193–8201.
[43] Li, C.; Yan, X.; Song, X. F.; Bao, W. Z.; Ding, S. J.; Zhang, D. W.; Zhou, P. WSe_2/MoS_2 and $MoTe_2$/$SnSe_2$ van der Waals heterostructure transistors with different band alignment. *Nanotechnology* **2017**, *28*, 415201.
[44] Jin, N.; Yu, R. H.; Chung, S. Y.; Berger, P. R.; Thompson, P. E.; Fay, P. High sensitivity Si-based backward diodes for zero-biased square-law detection and the effect of post-growth annealing on performance. *IEEE Electron Device Lett.* **2005**, *26*, 575–578.
[45] Park, S. Y.; Yu, R.; Chung, S. Y.; Berger, P. R.; Thompson, P. E.; Fay, P. Sensitivity of Si-based zero-bias backward diodes for microwave detection. *Electron. Lett.* **2007**, *43*, 295–296.
[46] DeRose, C. T.; Trotter, D. C.; Zortman, W. A.; Starbuck, A. L.; Fisher, M.; Watts, M. R.; Davids, P. S. Ultra compact 45 GHz CMOS compatible Germanium waveguide photodiode with low dark current. *Opt. Express* **2011**, *19*, 24897–24904.
[47] Alekseev, E.; Pavlidis, D. Large-signal microwave performance of GaN-based NDR diode oscillators. *Solid State Electron.* **2000**, *44*, 941–947.
[48] Abraham, N.; Murali, K.; Watanabe, K.; Taniguchi, T.; Majumdar, K. Astability versus bistability in van der Waals tunnel diode for voltage controlled oscillator and memory applications. *ACS Nano* **2020**, *14*, 15678–15687.
[49] Munsterman, G. T. Tunnel-diode microwave amplifiers. *APL Technol. Dig.* **1965**, *4*, 2–10.
[50] Shim, J.; Oh, S.; Kang, D. H.; Jo, S. H.; Ali, M. H.; Choi, W. Y.; Heo, K.; Jeon, J.; Lee, S.; Kim, M. et al. Phosphorene/rhenium disulfide heterojunction-based negative differential resistance device for multi-valued logic. *Nat. Commun.* **2016**, *7*, 13413.
[51] Jeon, J.; Kim, M. J.; Shin, G.; Lee, M.; Kim, Y. J.; Kim, B.; Lee, Y.; Cho, J. H.; Lee, S. Functionalized organic material platform for realization of ternary logic circuit. *ACS Appl. Mater. Interfaces* **2020**, *12*, 6119–6126.
[52] Brivio, J.; Alexander, D. T. L.; Kis, A. Ripples and layers in ultrathin MoS_2 membranes. *Nano Lett.* **2011**, *11*, 5148–5153.
[53] Jena, D. Tunneling transistors based on graphene and 2-D crystals.

Proc. IEEE **2013**, *101*, 1585–1602.

[54] Srivastava, P. K.; Hassan, Y.; Gebredingle, Y.; Jung, J.; Kang, B.; Yoo, W. J.; Singh, B.; Lee, C. Van der Waals broken-gap p–n heterojunction tunnel diode based on black phosphorus and rhenium disulfide. *ACS Appl. Mater. Interfaces* **2019**, *11*, 8266–8275.

[55] Qin, F. L.; Gao, F.; Dai, M. J.; Hu, Y. X.; Yu, M.; Wang, L.; Feng, W.; Li, B.; Hu, P. Multilayer InSe–Te van der Waals heterostructures with an ultrahigh rectification ratio and ultrasensitive photoresponse. *ACS Appl. Mater. Interfaces* **2020**, *12*, 37313–37319.

[56] Kim, Y. R.; Phan, T. L.; Shin, Y. S.; Kang, W. T.; Won, U. Y.; Lee, I.; Kim, J. E.; Kim, K.; Lee, Y. H.; Yu, W. J. Unveiling the hot carrier distribution in vertical graphene/h-BN/Au van der Waals heterostructures for high-performance photodetector. *ACS Appl. Mater. Interfaces* **2020**, *12*, 10772–10780.

[57] Wang, Q. S.; Wen, Y.; He, P.; Yin, L.; Wang, Z. X.; Wang, F.; Xu, K.; Huang, Y.; Wang, F. M.; Jiang, C. et al. High-performance phototransistor of epitaxial PbS nanoplate–graphene heterostructure with edge contact. *Adv. Mater.* **2016**, *28*, 6497–6503.

[58] Wen, Y.; Yin, L.; He, P.; Wang, Z. X.; Zhang, X. K.; Wang, Q. S.; Shifa, T. A.; Xu, K.; Wang, F. M.; Zhan, X. Y. et al. Integrated high-performance infrared phototransistor arrays composed of nonlayered PbS–MoS_2 heterostructures with edge contacts. *Nano Lett.* **2016**, *16*, 6437–6444.

[59] Yu, M. M.; Hu, Y. X.; Gao, F.; Dai, M. J.; Wang, L. F.; Hu, P. A.; Feng, W. High-performance devices based on InSe–$In_{1-x}Ga_xSe$ van der Waals heterojunctions. *ACS Appl. Mater. Interfaces* **2020**, *12*, 24978–24983.

[60] Zhou, X.; Hu, X. Z.; Zhou, S. S.; Song, H. Y.; Zhang, Q.; Pi, L. J.; Li, L.; Li, H. Q.; Lü, J. T.; Zhai, T. Y. Tunneling diode based on WSe_2/SnS_2 heterostructure incorporating high detectivity and responsivity. *Adv. Mater.* **2018**, *30*, 1703286.

[61] Li, A. L.; Chen, Q. X.; Wang, P. P.; Gan, Y.; Qi, T. L.; Wang, P.; Tang, F. D.; Wu, J. Z.; Chen, R.; Zhang, L. Y. et al. Ultrahigh-sensitive broadband photodetectors based on dielectric shielded $MoTe_2$/Graphene/SnS_2 p–g–n junctions. *Adv. Mater.* **2019**, *31*, 1805656.

[62] Wang, Z. X.; Wang, F.; Yin, L.; Huang, Y.; Xu, K.; Wang, F. M.; Zhan, X. Y.; He, J. Electrostatically tunable lateral $MoTe_2$ p–n junction for use in high-performance optoelectronics. *Nanoscale* **2016**, *8*, 13245–13250.

[63] Farzami, F.; Khaledian, S.; Smida, B.; Erricolo, D. Ultra-low power reflection amplifier using tunnel diode for RFID applications. In *Proceedings of 2017 IEEE International Symposium on Antennas and Propagation & USNC/URSI National Radio Science Meeting*, San Diego, CA, USA, 2017, pp 2511–2512.

[64] Park, C.; Duong, N. T.; Bang, S.; Nguyen, D. A.; Oh, H. M.; Jeong, M. S. Photovoltaic effect in a few-layer ReS_2/WSe_2 heterostructure. *Nanoscale* **2018**, *10*, 20306–20312.